Influence of solder condition on effective thermal conductivity of two-directional random fibres

Pore-scale simulation

Xiao, Tian; Zhang, Qiaoling; Yang, Xiaohu; Hooman, Kamel; Li, Guodong

DOI
10.1016/j.ijheatmasstransfer.2022.123715

Publication date
2023

Document Version
Final published version

Published in
International Journal of Heat and Mass Transfer

Citation (APA)
Xiao, T., Zhang, Q., Yang, X., Hooman, K., & Li, G. (2023). Influence of solder condition on effective thermal conductivity of two-directional random fibres: Pore-scale simulation. *International Journal of Heat and Mass Transfer*, *202*, Article 123715. https://doi.org/10.1016/j.ijheatmasstransfer.2022.123715

International Journal of Heat and Mass Transfer 202 (2023) 123715

Contents lists available at ScienceDirect

International Journal of Heat and Mass Transfer

journal homepage: www.elsevier.com/locate/hmt

Influence of solder condition on effective thermal conductivity of two-directional random fibres: Pore-scale simulation

Tian Xiao[a,b], Qiaoling Zhang[a], Xiaohu Yang[a,c,**], Kamel Hooman[d,*], Guodong Li[a]

[a] State Key Laboratory of Eco-hydraulics in Northwest Arid Region, Xi'an University of Technology, Xi'an 710048, PR China
[b] State Key Laboratory for Strength and Vibration of Mechanical Structures, School of Aerospace, Xi'an Jiaotong University, Xi'an 710049, PR China
[c] Institute of the Building Environment & Sustainability Technology, School of Human Settlements and Civil Engineering, Xi'an Jiaotong University, Xi'an 710049, PR China
[d] Department of Process and Energy, Delft University of Technology, Postbus 5, Delft 2600 AA, The Netherlands

ARTICLE INFO

Article history:
Received 19 September 2022
Revised 31 October 2022
Accepted 22 November 2022

Keywords:
Metal fibre materials
Effective thermal conductivity (ETC)
Numerical simulation
Solder joints

ABSTRACT

It is indicated that the solder joint of the metal fibrous materials is a critical factor impacting the heat conduction. To reveal the mechanism by which solder joint sizes, solder joint skips, solder flux materials, and filling media affect the thermal conductivity of fibres, pore-scale numerical simulation is employed to study the thermal transport in two-directional (2-D) random fibres. Satisfactory agreement with existing data validates the numerical model. The dimensionless effective thermal conductivity (ETC) of the porous fibres increases with the solder joint sizes. As the solder joint size (i.e., solder joint ratio) increases by 3.06%, the in-plane ($k_{e\text{-}in}$) and out-of-plane ($k_{e\text{-}out}$) dimensionless ETC increase by 9.0% and 437.2%, respectively. However, the solder joint skips will weaken the thermal conductivity of the fibres. For the same fibre, the ETC of the fibre increases as the thermal conductivity of solders increases. Further, when the dissimilarity in thermal conductivity between the filling medium and the fibre is reduced, the fibre is less affected by the solder joint skips. Finally, it should be supplemented that the in-plane and out-of-plane ETC ($k_{e\text{-}in}$ and $k_{e\text{-}out}$) of the fibre without any solder joint are reduced by an average of 14.3% and 98.8%, respectively.

1. Introduction

Metal fibrous materials (MFMs) have excellent characteristics such as lightweight, high porosity, strong damage resistance, heat transfer, high specific surface area, easy moulding, and low manufacturing cost [1–6]. MFMs have attracted extensive attentions in engineering applications, such as thermal management [7–11], ballistic protection [12,13], composite reinforcement [14,15], fuel cells [16–18], catalysts [19], enhanced thermal storage [20–22], and energy absorption [23,24]. For these engineering applications, the effective thermal conductivity (ETC) of MFM is a vital parameter that determines heat conduction capability [25,26]. However, the filament orientations of fibrous materials, e.g., two-directional (2-D) random fibres as the representative, result in different in-plane and out-of-plane features for the heat conduction and their ETCs. 2-D MFM is formed by stacking fibres layer by layer, where each layer of the fibres is randomly distributed in the plane.

MFMs have extremely complex structures due mainly to the entanglements and random arrangements in porous structures [27,28]. This makes it more difficult to determine their transport properties. To reveal the transport mechanism in MFM, different methods including theoretical analysis [29–31], numerical simulations [32–37], and experimental measurements [38–41] have been taken to characterize the fibre pore structures and to explore their transport properties.

Given the complicated pore structure of metal fibre materials, most theoretical models simplify the complicated porous structures into ideal periodic unit cells (UCs). Sadeghi et al. [29] proposed an analytical model to evaluate the ETC of the fibrous materials using cylindrical fibres with an equal spacing and uniform size. Hooman and Dukhan [42] also established a theoretical model based on a cubic arrays of cylinders to depict the transport properties of porous media. The model has good prediction accuracy. Similarly, Qu et al. [30] chose an octet-truss lattice UC to establish an analytical expression for the ETC of the isotropic fibres. In addition, a theoretical model for predicting the ETC of sintered fi-

** Corresponding author at: State Key Laboratory of Eco-hydraulics in Northwest Arid Region, Xi'an University of Technology, Xi'an 710048, PR China.
* Corresponding author.
E-mail addresses: xiaohuyang@xjtu.edu.cn (X. Yang), K.Hooman@tudelft.nl (K. Hooman).

https://doi.org/10.1016/j.ijheatmasstransfer.2022.123715

Nomenclature

Symbols

k	thermal conductivity ($W{\cdot}m^{-1}{\cdot}K^{-1}$)
k_e	effective thermal conductivity ($W{\cdot}m^{-1}{\cdot}K^{-1}$)
l	length (m)
L	length of heat conduction (m)
P	power of the top solder joints on the top surface (W)
q	heat flux (W/m^2)
R	thermal resistance (W/K)
S	cross-sectional area of solder joint (m^2)
S_{b-i}	ith bottom solder joint
S_{t-i}	ith top solder joint
T	temperature (K)
T_b	bottom surface temperature of the lower solder joints (K)
T_H	high temperature (K)
T_L	low temperature (K)
T_t	top surface temperature of the upper solder joints (K)
$\vec{V}$	velocity vector ($m{\cdot}s^{-1}$)
V_s	total volume of the fibres (m^3)
V_{SJ}	total volume of the solder joints (m^3)
V_{SJS}	total volume of the solder joint skips (m^3)

Greek symbols

φ	percentage of solder joint volume
ω	solder joint skip ratio
ε	porosity

Subscript

ave	average
e	effective parameter
f	fluid
i	ith
in	in-plane
out	out-of-plane
s	solid
sf	solder flux

Abbreviation

ETC	effective thermal conductivity
MFM	metal fibrous material
PCM	phase change material
RUC	representative unit cell
2-D	two-dimension

bres was developed by Sheng et al. [43]. However, these theoretical models ignored the remarkable influence of fibre pores with random distribution and various sizes upon heat transport. To this end, Xiao et al. [25] theorized the ETC of the randomly-distributed fibres by the fractal theory, providing an alternative approach for the theoretical analysis of the MFMs. Comparing their predicted results with the measurement results, the average relative deviations of in-plane and out-of-plane were 5.02% and 13.02% for aluminum fiber saturated with air, respectively. Although their results indicated that the solder joint of the MFM played a crucial role in affecting the heat transport, an in-depth analysis is lacking. In most theoretical studies, the geometries of the fibre materials are too convoluted to pay attention to the impact of solder joints on the ETC of the fibres.

To get closer to the real structures of the MFMs, numerical simulations are conducted to reconstruct their microporous structures. Pore-scale numerical simulation is a crucial way to reveal the transport properties of porous media [44–47]. For two-directional isotropic disordered MFMs, Volkov and Zhigilei [32] proposed a numerical framework for calculating the ETC. Wang et al. [33] predicted the ETC of the natural fibre materials by a lattice Boltzmann algorithm. Shirbani et al. [48] also developed a lattice Boltzmann model to simulate the heat conduction in porous media. In the view of Arambakam et al. [34], the porosity, diameter, and orientation of the fibres were the key factors affecting the ETC of the MFMs. Similarly, Huang et al. [35] simulated the heat conduction in the three-dimensional random fibres. Their simulation results were consistent with the experimental measurements. In addition, Fiedler et al. [49] and Opolot et al. [50] presented the thermal contact resistance can be not negligible in the heat conduction of porous media. In continuous studies, Ni et al. [36] numerically studied the inextricable link for the ETC of the MFMs to the microstructure. They reported that the ETC of the MFM was the smallest when the fiber orientation was perpendicular to the direction of heat conduction.

In experimental studies, Veyhl et al. [38] found that the layered structure of the MFM is one of the key factors in determining its ETC. Haruki et al. [39], Li and Qu [40] also found that the porosity, fibre length, and diameter significantly affected the ETC of the MFMs. According to Li and Qu [40], when the fiber diameter increased from 100 μm to 200 μm, the ETC decreased by 40.7%. Importantly, experiments by Li and Qu [40], and Yi et al. [41] confirmed that there were solder joints between each metal fibre. The thermal performance of sintered fibers in the flat-shaped heat pipes was reported by Maneemuang et al. [51]. A great deal of previous studies on the ETC of the fibres have focused on the pore size, porosity, fibre diameter, and orientation. However, the impact of solder joints upon the heat conduction characteristics and ETCs remain elusive.

To sum up, previous studies have yet paid little attention to the impact of the solder joints of the MFMs on the ETC in terms of theoretical analyses, numerical simulations, and experiments. Moreover, there is a lack of study to explain the mechanisms of how the solder joints affect the heat transport and the ETCs at pore scale. To this end, this study is intended to reveal the impact of solder joints on the thermal transport characteristics and the ETCs by the pore-scale numerical approach. A representative UC model for the anisotropic 2-D random MFM is built by reconstructing the topological and morphological micro features. Good agreement with the previous simulation and measurement data verifies the correctness and applicability of the established numerical model. Effects of the solder joint size, solder flux, and filling media on the in-plane and out-of-plane ETCs of the MFMs are explored. The heat conduction characteristics, mechanisms, and determinations on the contributions of the fibre solder joints to thermal transport pave the foundation of understanding and estimation on the ETCs for MFMs in engineering applications.

2. Numerical method

2.1. Representative structure

A scanning electron microscope (SEM) image of the MFM is shown in Fig. 1(a). As seen, MFM is fabricated by stacking randomly-distributed filaments layer by layer. To simplify the model, we assume that the axes of the 2-D fibrous structure are located in planes parallel to each other (see Fig. 1(b) and (c)), and the positions and orientations of the cylindrical, infinitely long fibers are randomly distributed in these planes. Fig. 1(b) depicts the reconstructed porous structure for the MFM according to the SEM image in Fig. 1(a). The axes of filaments are disordered and random in the horizontal plane. However, the actual structure of the metal fibre is extremely complex (see Fig. 1(a) and (b)), and it seems impractical to simulate the entire fibre structure directly.

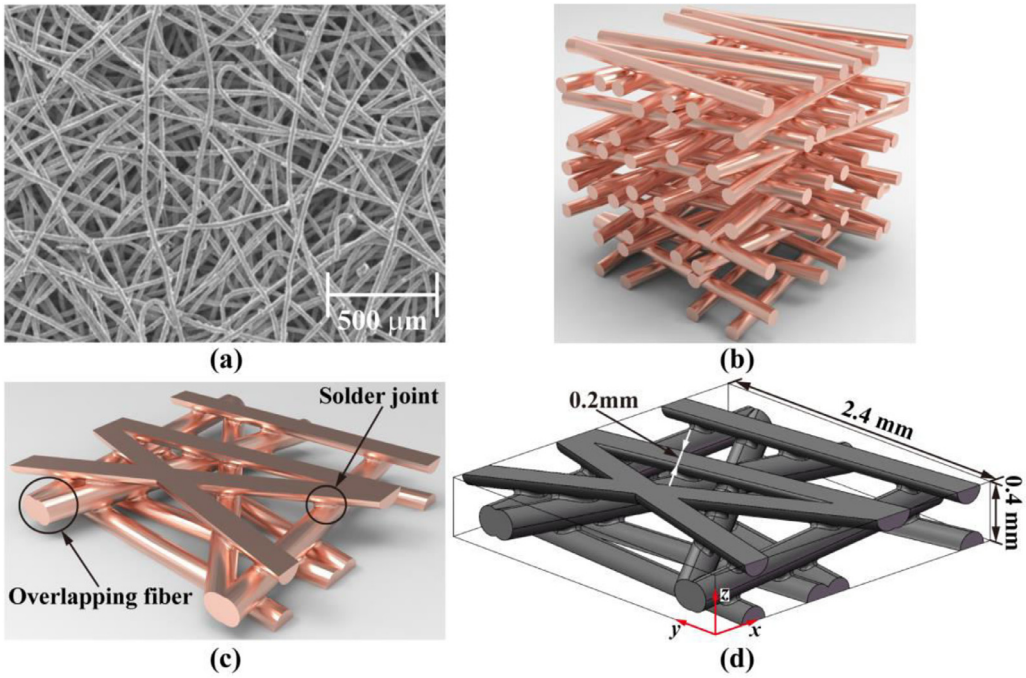

Fig. 1. 2-D random fibre geometric model: (a) metal fibre [30]; (b) schematic diagram of 2-D random metal fibre; (c) representative unit cell structure; (d) dimensions for the computational model.

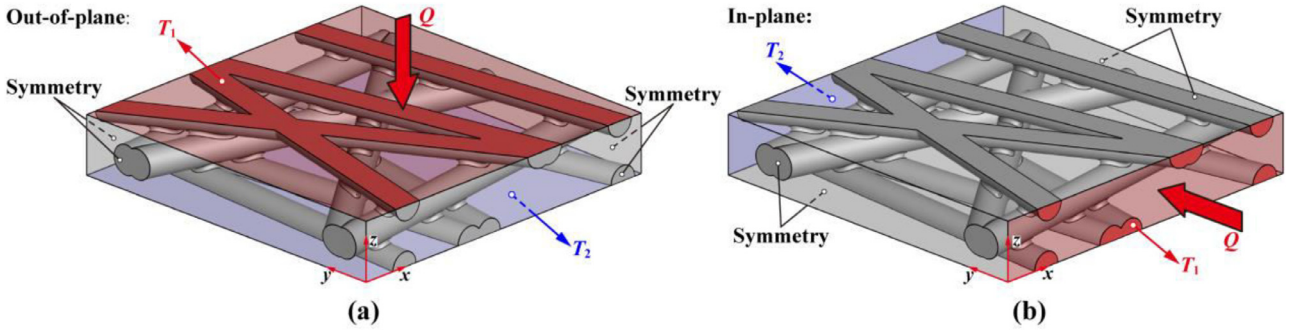

Fig. 2. Boundary conditions for the ETC: (a) out-of-plane; (b) in-plane.

Therefore, it is necessary to select a representative unit cell (RUC) that contains the main characteristics of the MFM. Fig. 1(c) displays the RUC, which is composed of one full layer fibres and two half-layer fibres. The inherent nature such as random distribution, overlap and contact of fibres has been well interpreted by the RUC. The fibre layers are in contact with each other by the solder joints. Furthermore, there exist overlaps between the randomly-distributed fibres in the same layer. Fig. 1(b) denotes that the length, width, and height of the RUC are separately 2.4 mm, 2.4 mm, and 0.4 mm, according to the previous study [39] that it is reasonable to set the diameter of representative structural fibres to 0.2 mm.

2.2. Effective thermal conductivity modelling

ANSYS-Fluent 19.1 is used for the pore-scale simulation, providing better understandings on the heat conduction mechanism of metal fibres at microporous scale. Since the fibres are randomly distributed in a layer-by-layer pattern, the joint conditions among various fibres are critical to heat conduction. In the current study, we consider only the heat conduction of the model and ignore the convection. Furthermore, the fluid in the model is stationary ($\vec{V} = 0$). Therefore, the governing equation is simply the energy equation.

Energy equation for solid phase:

$$\nabla \cdot (k_s \nabla T_s) = 0 \tag{1}$$

Energy equation for fluid phase:

$$\nabla \cdot \left(k_f \nabla T_f\right) = 0 \tag{2}$$

where, k_s and k_f represent the ETC of solid phase and fluid phase, respectively; T_s and T_f denote the temperature of solid phase and fluid phase, in respective. In addition, Fig. 2(a) and (b) demonstrate the boundary conditions for the out-of-plane and in-plane modelling on the ETC. In Fig. 2(a), the temperature is set to 300 K (i.e., $T_1 = 300$ K) in the top z-direction, and the bottom surface temperature in the z-direction is set to 299 K (i.e.,$T_2 = 299$ K). Similarly, the front surface temperature in the y-direction is 300 K (i.e.,$T_1 = 300$ K), and the rear surface temperature in the y-direction maintains at 299 K (i.e.,$T_2 = 299$ K) in Fig. 2(b). The remaining surfaces in Fig. 2(a) and (b) are symmetric. Finally, the residuals of the energy equation are set to 10^{-10} to ensure the convergence of the calculation.

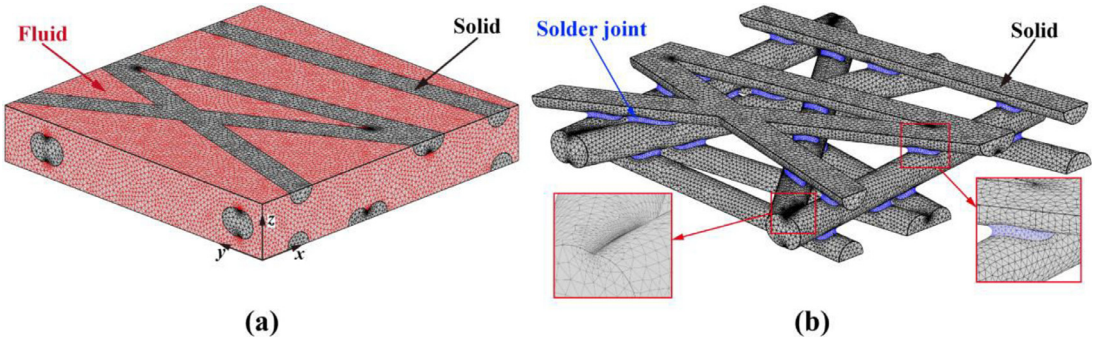

Fig. 3. Representative mesh: (a) assembly; (b) solid phase.

Table 1
Physical parameters for MFM.

Property	Copper	Aluminum	Nickel	Steel	Tin	Plumbum
Density ($kg \cdot m^{-3}$)	8978	2719	8900	8030	5770	10,200
Specific heat capacity ($J \cdot kg^{-1} \cdot K^{-1}$)	381	871	460.6	502.48	213	100
Thermal conductivity ($W \cdot m^{-1} \cdot K^{-1}$)	398	202.4	91.74	16.27	63.2	33
Property	Sn63[a]	Air	Water	PCM1[b] [52]	PCM2[c] [53]	N/A
Density ($kg \cdot m^{-3}$)	8400	1.225	998.2	1481	875	N/A
Specific heat capacity ($J \cdot kg^{-1} \cdot K^{-1}$)	167	1006.43	4182	3540	2516	N/A
Thermal conductivity ($W \cdot m^{-1} \cdot K^{-1}$)	50	0.0242	0.6	0.911	3	N/A

Note:
[a] Sn63: 106 (Sn63) Sn-Pb Solder Alloy;
[b] PCM1: $CaCl_2 \cdot 6H_2O$(95%)+$Mg(NO_3) \cdot 6H_2O$(5%) [52];
[c] PCM2: $CaCl_2 \cdot 6H_2O$/EG [53].

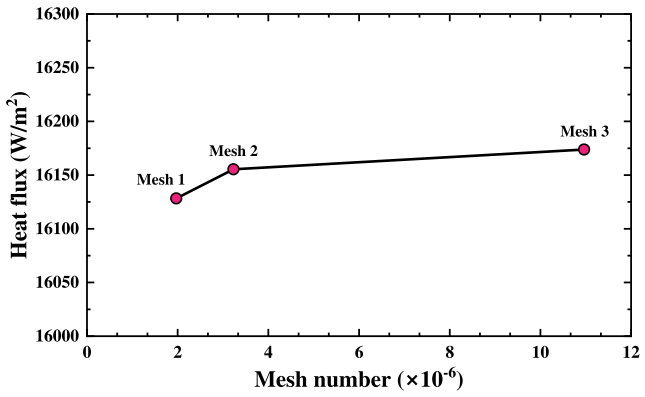

Fig. 4. Mesh independence verification.

Fig. 3 demonstrates the representative mesh and corresponding computational domain for the numerical problem. As indicated in Fig. 3, the red and grey domain denote the fluid phase and solid phase, respectively. Unstructured mesh is generated using the ANSYS-ICEM CFD 19.1 with locally refined on the solder joints and overlaps (see Fig. 3(b)). In particular, the solder joints are highlighted as blue in Fig. 3(b). Different metals are utilized to fabricate the MFM and their thermophysical parameters are summarized in Table 1.

2.3. Mesh independence verification

To verify the independence of mesh on numerical calculations, three various meshes with 1,969,655 (Mesh-1), 3,231,362 (Mesh-2), and 10,963,715 (Mesh-3) are tested. As demonstrated in Fig. 4, there seems to be a very small difference (0.11%) in heat flux between Mesh-2 and Mesh-3. Therefore, considering the computational cost and reliability, the number of mesh for subsequent numerical simulations is not less than the number of Mesh-2.

3. Simulation validation

To verify the accuracy of the pore-scale simulation, the in-plane and out-of-plane ETC of the air-saturated copper fibre are compared with measurements and simulations in literature [35,39] in Fig. 5(a) and (b), in respective. In the current study, the uncertainty for the thermal conductivity of the experimental data is 5.0% [39]. The effective thermal conductivity k_e can be calculated by the following equations:

$$k_e = \frac{q_{ave} l}{T_H - T_L} \tag{3}$$

where, q_{ave} is the average heat flux of the high temperature surface; l represents the thickness of the metal fibre (length between T_H and T_L); besides, T_H and T_L denote the high temperature and the low temperature, respectively. As noticed, the current simulation has a satisfactory agreement with the two sources in Fig. 5. This demonstrates the reasonability and feasibility of the established numerical models that are based on the RUC shown in Fig. 1(c). Besides, as noted in Fig. 5, the ETCs of the 2-D MFM are different along the in-plane and out-of-plane directions. This phenomenon will be analyzed in the subsequent subsections.

4. Results and discussion

4.1. Effect of solder joint size on ETC

This section discusses the effect of the solder joint size on the ETC of the MFM. Each solder joint is intact without solder joint skips. A ratio (φ) of the total volume of the solder joint to that of the fibres is introduced, with a definition of

$$\varphi = \frac{V_{SJ}}{V_s} \times 100\% \tag{4}$$

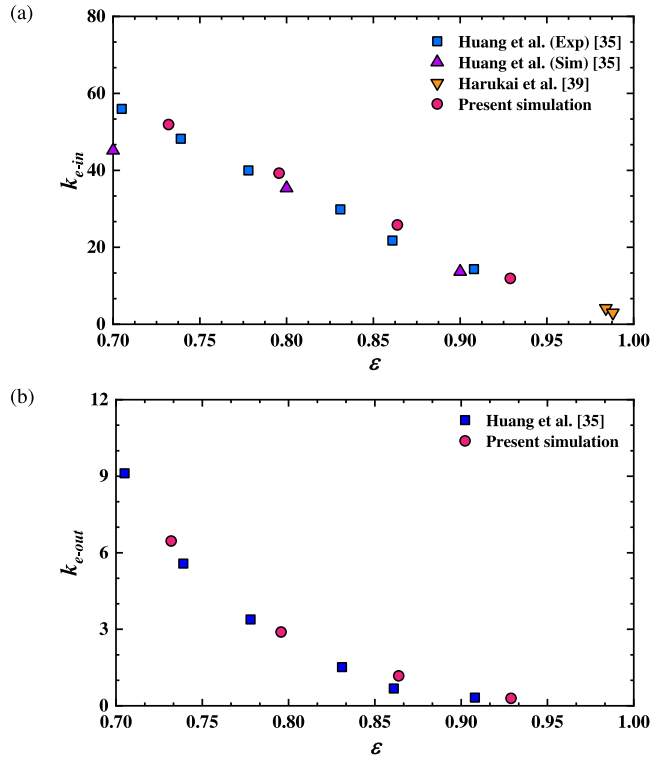

Fig. 5. Comparison of numerical results with previous measurement data [35,39] and simulation data [35]: (a) in-plane 2-D MFM; (b) out-of-plane 2-D MFM.

where, V_{SJ} and V_s denote the total volume of the solder joint and the fibres, respectively. The solder joint ratio does not exceed 3.5% in this study for the following reasons: (i) in the engineering fabrication routine, previous studies [54,55] have evinced that MFM are fabricated within 5% solder flux ($\varphi = 5\%$); (ii) excessive solder flux will cause multiple solder joints, forming overlap or weld flash; (iii) in the current simulation model (see Fig. 1(b) and (c)), some solder joints overlap when the sintered flux usage exceeds 3.5%.

Fig. 6 demonstrates the effect of solder flux ratio on the in-plane ($k_{e\text{-}in}$) and out-of-plane ($k_{e\text{-}out}$) dimensionless ETC for different metal fibre materials. A higher solder flux ratio leads to a bigger solder joint. The solder joint size causes a remarkable influence upon both $k_{e\text{-}in}$ and $k_{e\text{-}out}$. As seen, both . Compared with $k_{e\text{-}in}$, solder joint size makes greater contribution to $k_{e\text{-}out}$. When φ merely increases from 0.08% to 3.06%, $k_{e\text{-}out}$ increase by 437.23%; while this increment ratio is only 9.04% for $k_{e\text{-}in}$. It evinces that the solder joint size plays a critical role in determining heat conduction across the micro structure in MFM. In addition, the influence of metal materials (copper, aluminum, nickel, and steel) on the ETC is justified. As demonstrated, except for the steel with much lower thermal conductivity than other competing metallic materials, copper, aluminum, and nickel fibrous materials have much at one value of the ETC. Besides, the variation of solder joint size has the same influence on $k_{e\text{-}in}$ and $k_{e\text{-}out}$ for porous fibres with different metal materials.

To further reveal the impact of the solder joint size on the out-of-plane heat conduction characteristics, Figs. 7 and 8 compare the distribution of heat flux and temperature for the out-of-plane heat conduction in copper porous fibres with different solder joint sizes, respectively. Three solder ratios (0.37%, 1.55%, and 3.06%) are considered in Fig. 7, with the red areas in the local enlargement of the UC in Fig. 7(a1)–(c1) denoting the solder joints. As seen, a larger solder flux ratio causes a bigger solder joint. With high temperature imposed on the top of the UC, heat conduction occurs across the three layers of fibres. As found in Fig. 7, much higher heat flux is concentrated in the solder joint, compared to the other areas of the same fibre. The larger the solder joint (the higher solder ratio), the higher the heat flux. Heat conduction is obliged to pass through the fibre layers along the out-of-plane direction. Hence the solder joints between each fibre layer play a bridge role in transporting thermal energy. When the size of the solder joint increases, the cross-sectional area of the solder joint increases accordingly. According to the thermal resistance formula ($R = L/(k_{sf}S)$), an increase in the cross-sectional area S of solder joint results in a decrease in the thermal resistance R of the solder joint when the length L of the heat conduction and the thermal conductivity k_{sf} of the solder joint remain constant. With the reduced thermal resistance of the solder joint, heat is more easily conducted through the solder joint. Therefore, the larger size solder joints in Fig. 7 have higher heat flux. Comparably, the in-plane heat conduction is primarily along the direction of the fibres. Therefore, the solder joint size exerts a weaker influence on in-plane heat conduction than that for the out-of-plane heat conduction. In Fig. 8, the temperature distributions of the solder joints with various sizes are almost the same. It indicates that the effect of solder joint size on the temperature distribution is not obvious in the out-of-plane thermal

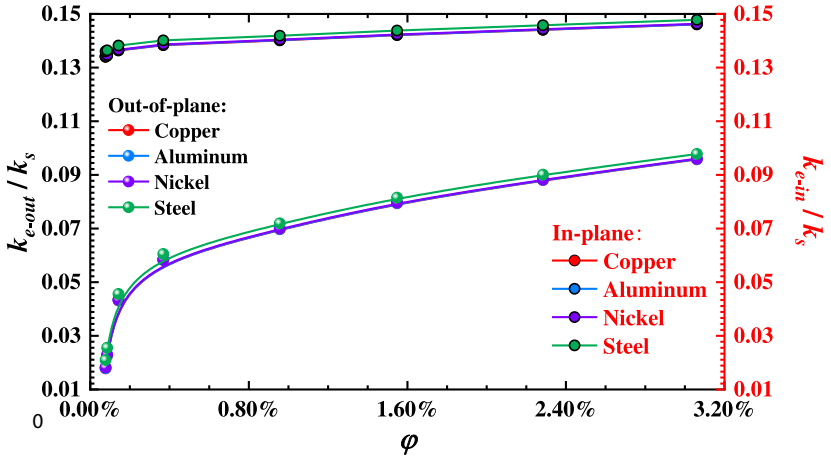

Fig. 6. Effect of solder flux ratio on in-plane ($k_{e\text{-}in}$) and out-of-plane ETCs.

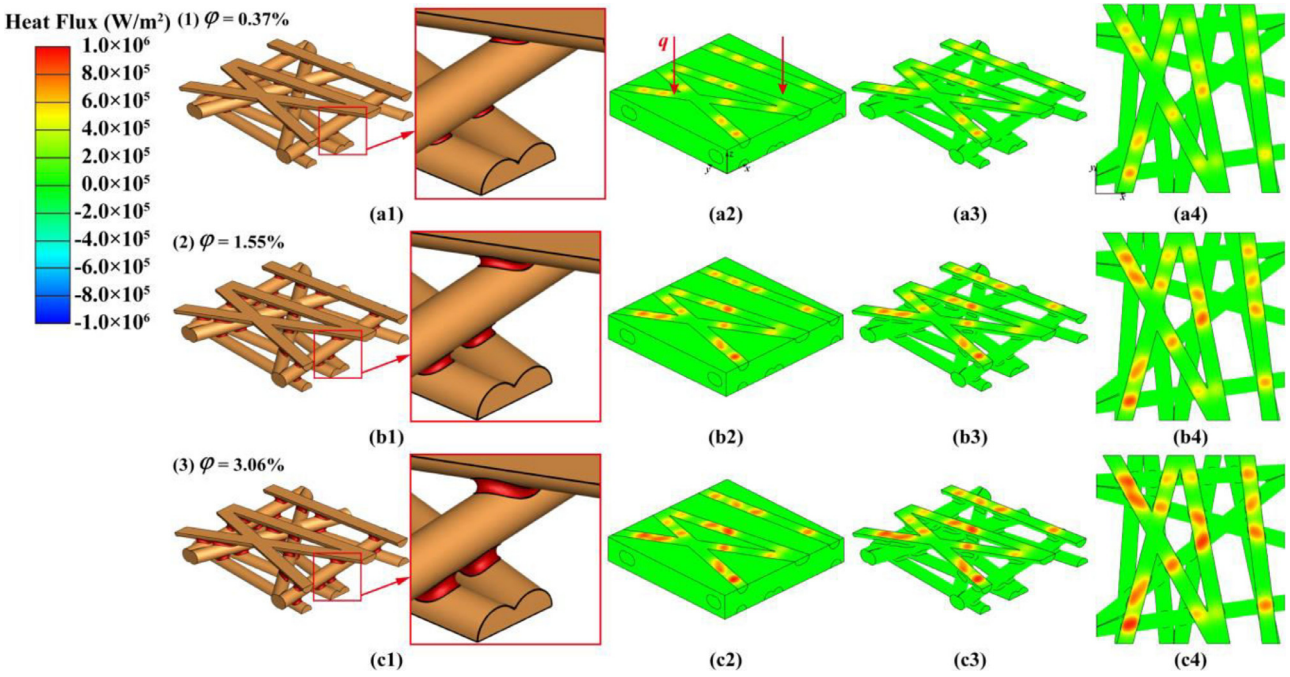

Fig. 7. Heat flux distribution for 2-D copper fibre with different sizes of solder joints: (a) $\varphi = 0.37\%$; (b) $\varphi = 1.55\%$; (c) $\varphi = 3.06\%$.

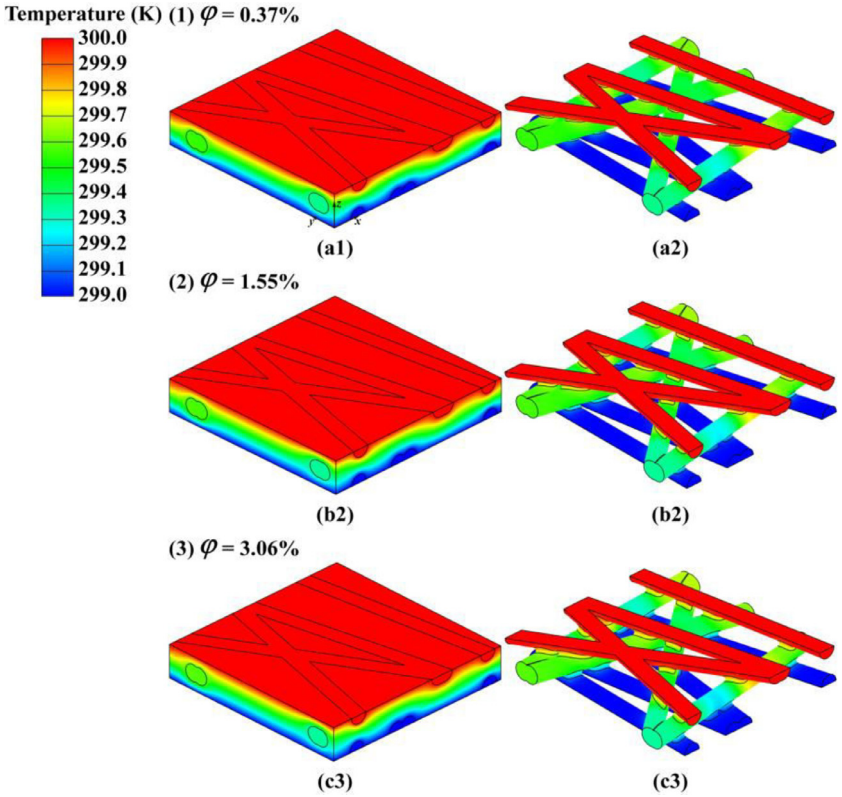

Fig. 8. Temperature distribution for 2-D copper fibre with different solder joint sizes: (a) $\varphi = 0.37\%$; (b) $\varphi = 1.55\%$; (c) $\varphi = 3.06\%$.

conduction. However, as φ increases from 0.37% to 3.06%, $k_{\text{e-out}}$ of the copper porous fibres increases by 65.5%.

4.2. Effect of solder joint skips

To further reveal the impact of the solder joints on the ETC of the MFM, this section focuses on analyzing the correlation between the ETC of the MFM and the number of the solder joint skips. Solder joint skips commonly happen when soldering metals. It is a kind of weld defect that significantly affects both the mechanical and thermal performance of the MFM with subject to thermal-mechanical loadings. Fig. 9(a) and (b) separately manifest the RUC structure with complete solder joints and the one with solder joint skips. In particular, the closest solder joints on the up-

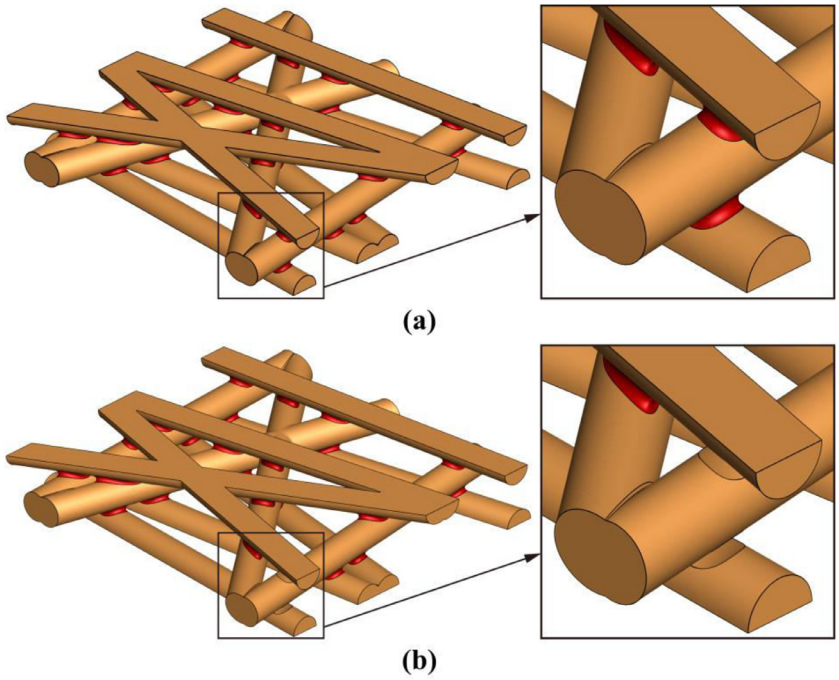

Fig. 9. Solder joint diagram: (a) complete solder joints; (b) solder joint skips.

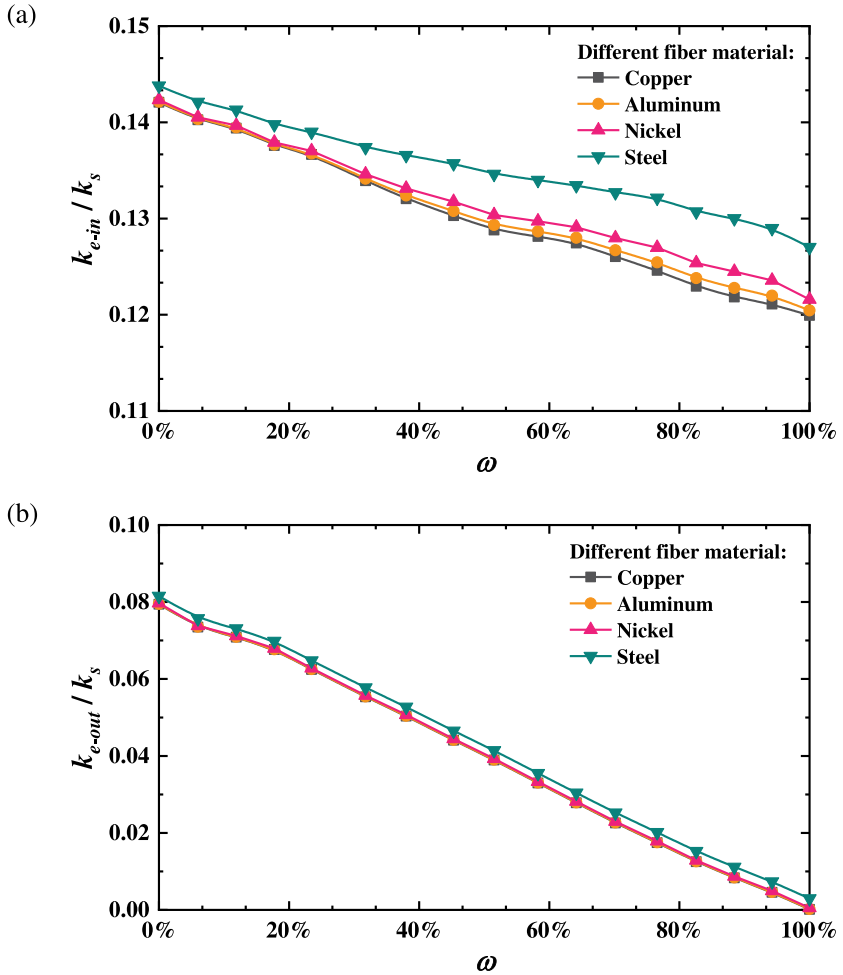

Fig. 10. Effect of solder joint skips on dimensionless ETC: (a) in-plane; (b) out-of-plane.

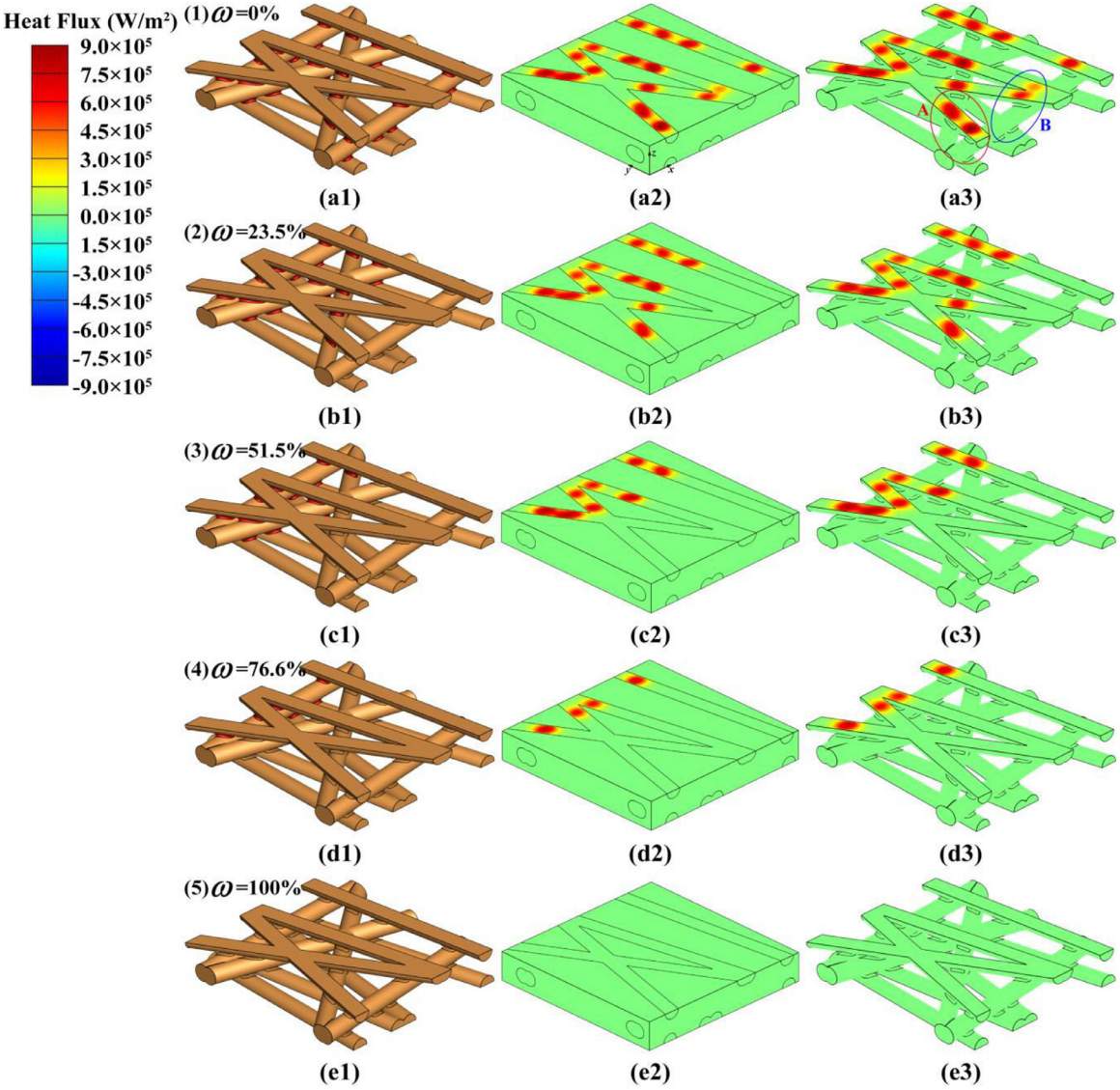

Fig. 11. Heat flux distribution for 2-D copper fibre with the different volume percentage of solder joint skips: (a) $\omega = 0\%$; (b) $\omega = 23.5\%$; (c) $\omega = 51.5\%$; (d) $\omega = 76.6\%$; (e) $\omega = 100\%$.

per and lower layers are skipped together in the z-direction of the RUC in Fig. 9(b).

To determine quantitatively the solder joint skips, a parameter named solder joint skip ratio (ω) is introduced:

$$\omega = \frac{V_{SJS}}{V_{SJ}} \times 100\% \tag{5}$$

where, V_{SJS} and V_{SJ} represent the volume of the solder joint skips and the total solder joints, in respective. When ω is equal to 0% ($\omega = 0\%$), all solder joints are intact. With it reaching 100% ($\omega = 100\%$), there exist no solder joints.

Fig. 10 depicts the variation of $k_{e\text{-}in}$ and $k_{e\text{-}out}$ as a function of the solder joint skip ratio. As seen, both $k_{e\text{-}in}$ and $k_{e\text{-}out}$ decrease with an increase in ω, demonstrating an approximately linear fashion. $k_{e\text{-}in}$ decreases by 15.60%, 15.27%, 14.57%, and 11.67% for copper (Cu), aluminum (Al), nickel (Ni), and steel fibres as ω increases from 0% to 100%, respectively. However, $k_{e\text{-}out}$ of the Cu, Al, Ni, and steel fibres separately decreased by 99.84%, 99.70%, 99.34% and 96.38% as ω increases from 0% to 100%. It displays that the impact of solder joint skips on the dimensionless ETC is weakened when the conductivity of the fibre material is smaller. It is noteworthy in Fig. 10 that the impact of solder joint skips on in-plane heat conduction is much smaller than out-of-plane heat conduction. The primary physical reason is that the out-of-plane heat conduction between each fibre layer is mainly through the solder joints, whereas the in-plane heat conduction is chiefly along the direction of the fibres in the same plane. When the solder joint is skipped, the out-of-plane heat conduction is hindered. The low thermal conductivity medium (typically the filling fluid) at the solder joint skips is not conducive to heat conduction. Therefore, the out-of-plane dimensionless ETC diminishes remarkably with the solder joint skips.

To supplementary visualize the effect of the solder joint skips on the out-of-plane heat conduction, the heat flux distribution and temperature field of the copper fibres are compared in Figs. 11 and 12, respectively. An increase in the number of solder joint skips results in an increase in the solder joint skip ratio (ω). In Fig. 11, the left column demonstrates the computational models with and without solder joint skips. Five solder joint skip ratios are compared regarding the heat flux distribution on the metal fibres and the corresponding filling fluids. The heat flux in the areas where the solder joint is intact is much greater than the areas with the

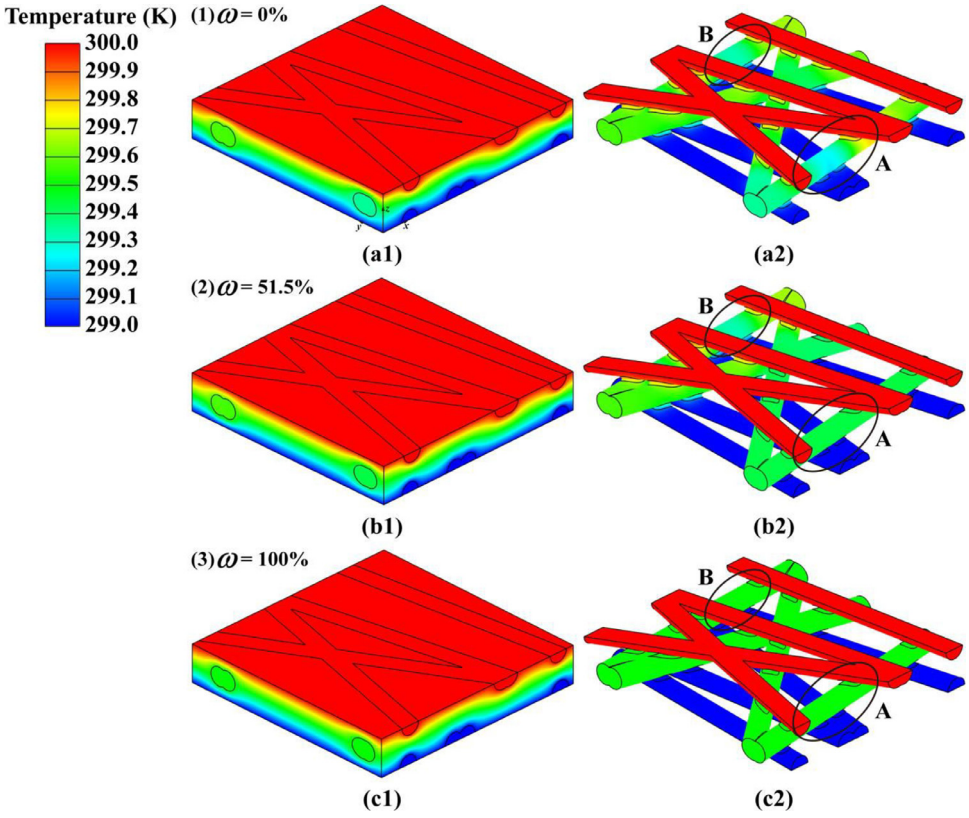

Fig. 12. Temperature distribution for 2-D copper fibre with the different volume percentage of solder joint skips: (a) $\omega = 0\%$; (b) $\omega = 51.5\%$; (c) $\omega = 100\%$.

solder joint skips (see the 2nd and 3rd column in Fig. 11). For the areas of solder joint skips, the heat flux in the corresponding areas is significantly reduced, and there is no obvious difference from the surrounding areas. It further indicates that the solder joints play a substantial role in enhancing out-of-plane heat transfer, in consistence with the continuously-decreasing trend of $k_{\text{e-out}}$ as a function of ω. Especially, when the solder joints are intact ($\omega = 0\%$), the heat flux in area A is much larger than that in area B in Fig. 11(a3). This is due to the fact that the upper and lower solder joints in area A are closer than those in area B, thereby providing an easier way for heat conduction. Moreover, the solid solder joint is an essential factor affecting the out-of-plane heat conduction. When the solder joints are skipping, the medium at the solder joint skips becomes the filling fluid. Thus, the thermal conductivity at the solder joint skips decreases dramatically. Based on the thermal resistance equation ($R = L/(k_{sf}S)$), an apparently decrease in the thermal conductivity k_{sf} of solder joint and an corresponding increase in the length L of the heat conduction lead to an increase in the thermal resistance R of the solder joint when the cross-sectional area S of the solder joint is fixed. With the increased thermal resistance of the solder joint, heat is more difficult to conduct through the solder joint skips. Therefore, the heat flux decreases sharply at the solder joint skips (see Fig. 11). The temperature distribution of the solder joint skips also displays apparent dissimilarity in Fig. 12. In the regions where the solder joints exist, the temperature gradient of the intermediate layer fibres in the z-direction is larger. In contrast, the temperature gradient in the regions with the solder joint skips decreases (see areas A and B in Fig. 12(a2)). When the solder joint skips ratio reaches 51.5% ($\omega = 51.5\%$) (see Fig. 12(b2)), the temperature gradient of the middle-layer fibre in area A with the solder joint skips is dramatically changed, while that in area B remains almost unchanged compared with the intact solder joints ($\omega = 0\%$) in Fig. 12(a2). The main reason is that there are some solder joint skips in area A, while the solder joints in area B are unimpaired (here $\omega = 51.5\%$). Similarly, without any solder joint (i.e., $\omega = 100\%$), the temperature gradients of the middle-layer fibre in area A and B are remarkably reduced compared with the intact solder joints (i.e., $\omega = 0\%$). This phenomenon is caused by the constant temperature of the top and bottom surfaces in the z-direction during the simulation. The higher thermal conductivity leads to a larger local temperature gradient in the middle layer of the fibres. Therefore, the temperature gradient in the area where the solder joint exists is larger.

Meanwhile, it should be specially noted that the heat flux distributions in different solder joint regions are various in Fig. 11 without the solder joint skips ($\omega = 0\%$). The thermal resistance of the different solder joints are calculated to quantify the dissimilarity in the contribution of the various solder joints. The thermal resistance formula is expressed as:

$$R_i = \frac{T_{t-i} - T_{b-i}}{P_i} \tag{6}$$

where, T_t and T_b are the top surface temperature of the upper solder joints and the bottom surface temperature of the lower solder joints in the z-direction; P is the power of the top solder joints on the top surface along the z-direction; i denotes the ith solder joint. As illustrated in Fig. 13(a), S_{t-i} represents the ith top solder joint and S_{b-i} denotes the ith bottom solder joint. The detailed numbering of the top and bottom solder joints are documented in Fig. 13(b) and (c), in respective. In addition, R_i is the thermal resistance between the ith top solder joint and the ith bottom solder joint (see Fig. 13(a)). For instance, R_2 depicts the thermal resistance between the 2nd top solder joint (S_{t-2}) and the 2nd bottom solder joint (S_{b-2}) in Fig. 13(a). Further, Fig. 13(d) demonstrates the distri-

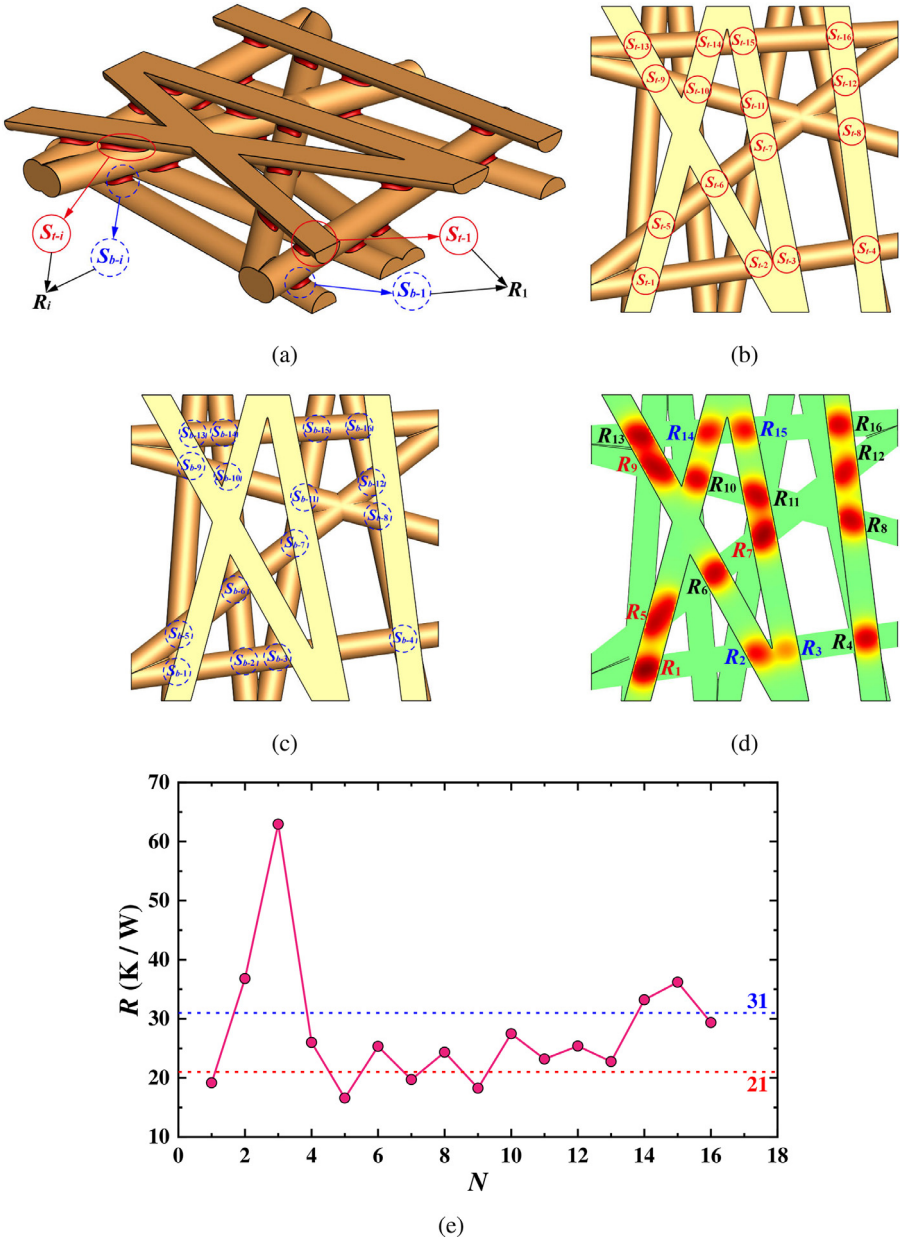

Fig. 13. Fibre solder joints: (a) schematic diagram of solder joints distribution; (b) distribution and numbering of top solder joints; (c) distribution and numbering of bottom solder joints; (d) thermal resistance distribution between top and bottom solder joints; (e) thermal resistance of solder joints.

bution of each thermal resistance for the solder joints. The gradation and range of color indicate the value of the thermal resistance.

To analyze the thermal conductivity between the top and corresponding bottom solder joints, Fig. 13(e) compares the thermal resistance of the different solder joints. The thermal resistance of different solder joints is diverse in Fig. 13(e). However, it can be divided into three parts according to the different thermal resistances: the first part of the solder joints (red number areas 1, 5, 7, and 9 in Fig. 13(d)) with thermal resistance less than 21 K/W (denoted as solder joint I); then the second part of solder joints (blue number area 2, 3, 14, and 15 in Fig. 13(d)) with thermal resistance greater than 31 K/W (marked as solder joint II); the last part is the rest of the solder joints with thermal resistance in the range of 21 K/W to 31 K/W (labelled as solder joint III). The heat flux distribution diagram without the solder joint skips ($\omega = 0\%$) in Fig. 13(d) demonstrates that the heat flux in the solder joint I is much higher, and the heat flux in the solder joint II area is a bit lower. The major reason for this difference is that the distances between the corresponding solder joints of the upper and lower layers are different. It can be noticed that the distance between the upper and lower solder joints of red number areas (1, 5, 7 and 9) is smaller, and thus the distance of heat conduction is shorter. In addition, the heat conduction distance of the upper and lower solder joints for the blue number areas (2, 3, 14, and 15) is much greater than that of the other upper and lower solder joints. Therefore, the heat flux in blue number areas (2, 3, 14, and 15) is remarkably reduced.

4.3. Thermal conductivity of solder flux

The solder joints size and quality for the fibres are vital factors affecting the out-of-plane heat conduction. The solder joints discussed in the previous sections are the same material as the fibres. In practice, the solder of the fibre is often not the same

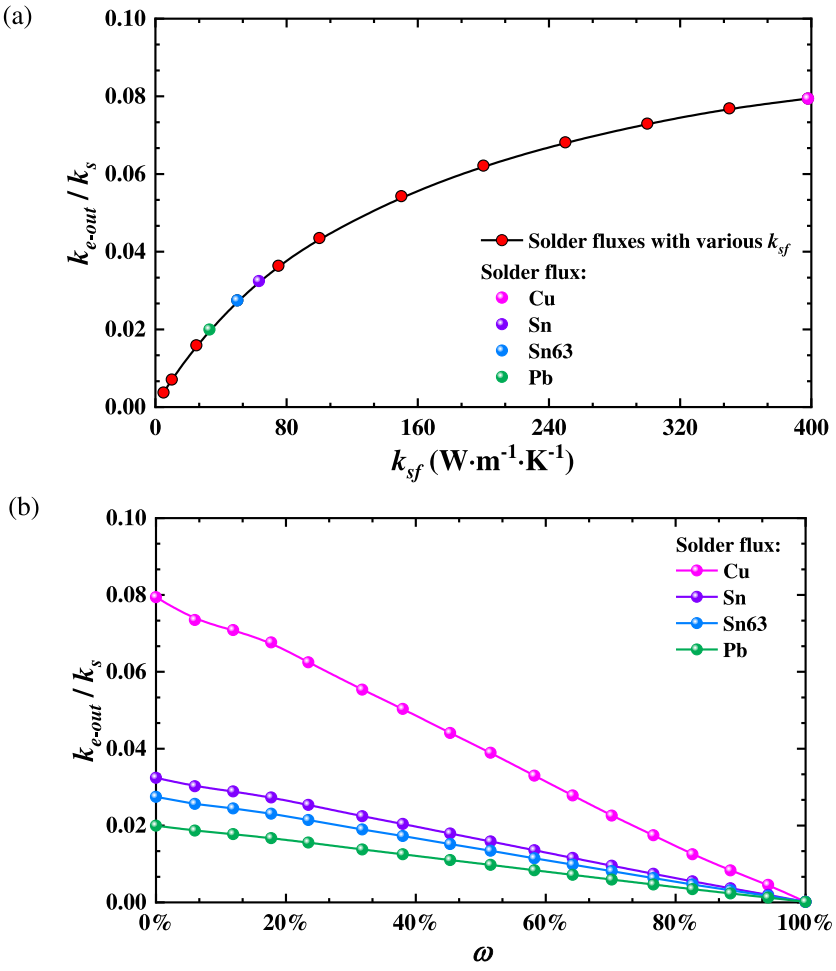

Fig. 14. (a) Out-of-plane dimensionless ETC of the copper fibres with various solder flux; (b) Out-of-plane dimensionless ETC of the fibres as a function of the solder joint skips.

composition as the fibre; hence the thermal conductivity of solders and fibres may be inconsistent. This section discusses the influence of different thermal conductivity of solder joints upon the out-of-plane heat conduction.

Fig. 14 indicates the effect of solder joint with different thermal conductivity on the out-of-plane dimensionless ETC of the fibre ($k_{\text{e-out}}$). Although $k_{\text{e-out}}$ increases steadily with the solder joint thermal conductivity for the intact solder joints in Fig. 14(a), the relationship is nonlinear. When the conductivity of the solder joint material is less than 150 $\text{W}\cdot\text{m}^{-1}\cdot\text{K}^{-1}$ (i.e., $k_{sf} \leqslant 150\text{W}\cdot\text{m}^{-1}\cdot\text{K}^{-1}$), the variation range of $k_{\text{e-out}}$ occupies 66.8% of the entire variation range for the copper fibre. It demonstrates that it has a distinct impact on $k_{\text{e-out}}$ when k_{sf} is less than 150 $\text{W}\cdot\text{m}^{-1}\cdot\text{K}^{-1}$. Therefore, the solder flux is a non-negligible element that affects the out-of-plane heat conduction of the MFM. Although $k_{\text{e-out}}$ of the copper fibre increases with the thermal conductivity for the solder joint, the influence of the solder joint thermal conductivity on the overall out-of-plane heat conduction of the fibres is weakened. For four different solder joint materials, the influence of the solder joint skips on $k_{\text{e-out}}$ is shown in Fig. 14(b). $k_{\text{e-out}}$ of the copper fibres with different solder joint materials decreases with the increase in the solder joint skips ratio (ω). Referring to Table 1, it can be uncovered that the smaller the thermal conductivity of the solder joints, the smaller the $k_{\text{e-out}}$ for copper fibre. Besides, it should also be noted that the impact of solder joints with low thermal conductivity on $k_{\text{e-out}}$ is weakened. When the main component of the solder joint is copper, $k_{\text{e-out}}$ of the copper fiber with the solder joint skips decays the fastest (Fig. 14(b)). Conversely, as the solder joint is mainly composed of Plumbum, the declining rate of $k_{\text{e-out}}$ with the solder joint skips is the slowest. For solder joints with Cu, Sn, Sn63, or Pb, the declining rate (slope of the curve) of $k_{\text{e-out}}$ caused by the solder joint skips is approximately 0.079, 0.032, 0.027, and 0.020, respectively.

To completely analyze the influence of the solder joints with various thermal conductivities on the out-of-plane heat conduction, Figs. 15 and 16 compare the heat flux distribution and temperature distribution of the RUCs. Fig. 15(a1)–(c1), and (d1) are the schematic diagrams of solder joints with different thermal conductivities, wherein solder joints with different colors represent different thermal conductivities. The blue, green, yellow, and red solder joints represent the thermal conductivities from low to high (see the first column of Fig. 15). The RUC has complete solder joints in Figs. 15 and 16. The heat flux of the solder joint areas is not apparently distinct from the surrounding areas when the thermal conductivity of the solder joint material is equal to 50 $\text{W}\cdot\text{m}^{-1}\cdot\text{K}^{-1}$ ($k_{sf} = 50\text{W}\cdot\text{m}^{-1}\cdot\text{K}^{-1}$). Currently, only the thermal conductivity of the solder flux is different, while the length L of the heat conduction and the cross-sectional area S of the solder joint remain constant. By the thermal resistance formula ($R = L/(k_{sf}S)$), solder fluxes with different thermal conductivity (k_{sf}) lead to variations in the thermal resistance of the corresponding solder joint. Therefore, when k_{sf} increases, the heat flux of the solder joint areas increases

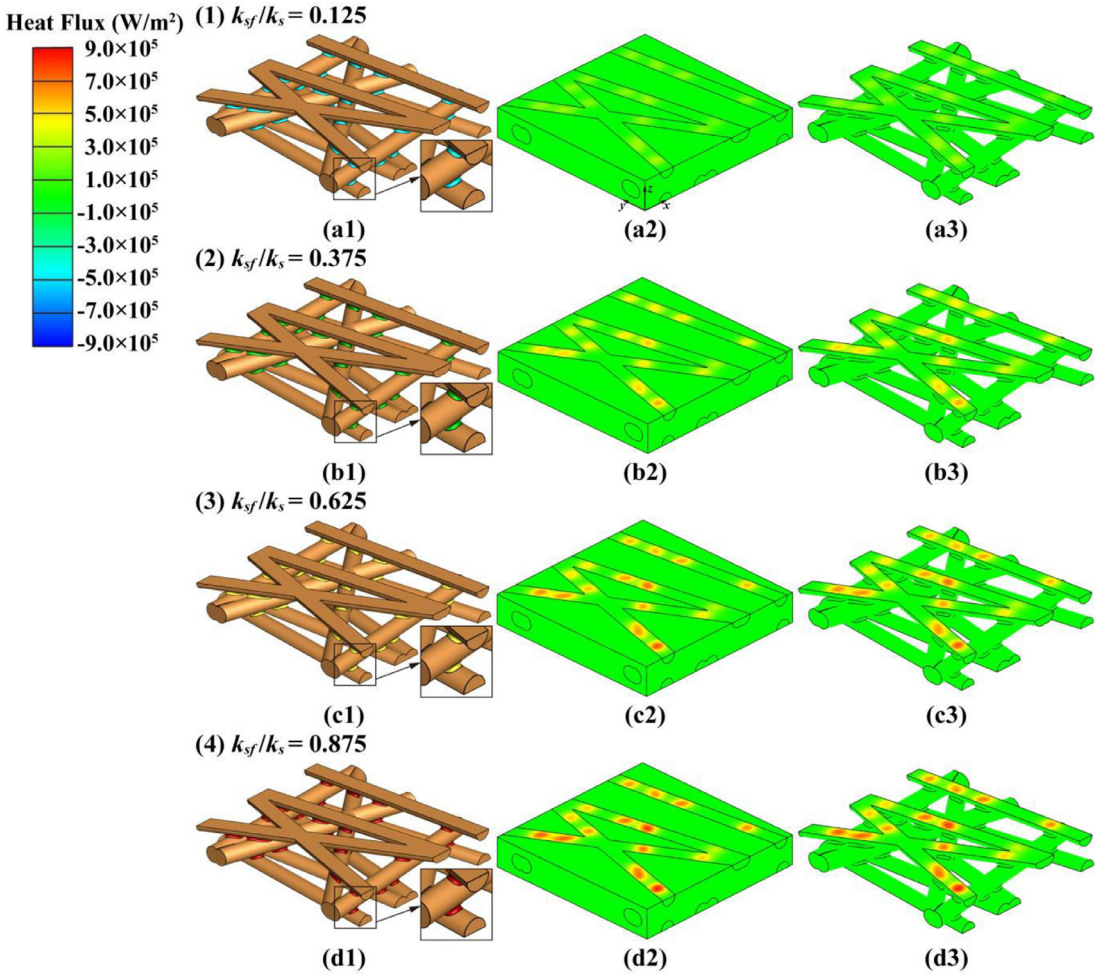

Fig. 15. Heat flux distribution for 2-D copper fibre with different thermal conductivity of solder joints: (a) $k_{sf}/k_s = 0.125$; (b) $k_{sf}/k_s = 0.375$; (c) $k_{sf}/k_s = 0.625$; (d) $k_{sf}/k_s = 0.875$.

accordingly, exacerbating the difference between the heat flux of the solder joint areas and the surrounding areas. This demonstrates that the thermal conductivity of solder joints is one of the vital factors influencing the out-of-plane heat conduction of the fibres. Therefore, improving the thermal conductivity of the solders is a meaningful measure to promote the out-of-plane heat conduction of fibres. Furthermore, the temperature gradient of the intermediate layer fibres between the upper and lower solder joints increases as the thermal conductivity of the solder joints approaches that of the fibre material (see region A in Fig. 16). This is chiefly because the high thermal conductivity of the solder joints facilitates heat conduction between the fibre layers.

4.4. Different filling fluids

MFMs filled with different fluids such as air, water, and phase change material (PCM) have distinctive engineering scenarios. To address this issue, this section focuses on studying the impact of different filling fluids upon $k_{\text{e-out}}$ of the MFMs with solder joint skips. For the solder joint skips, Fig. 17(a)–(d) severally compare the relationship between $k_{\text{e-out}}$ of the fibres and the filling fluids. Four kinds of MFMs including copper, aluminum, nickel, and steel are considered. As demonstrated in Fig. 17, there exists a steady decline trend of $k_{\text{e-out}}$ as ω increases. Moreover, the filling fluid with higher thermal conductivity can considerably promote $k_{\text{e-out}}$ for the same fibre. The smaller difference in thermal conductivity between the fibres and the filler medium makes the solder joint skips have less impact on $k_{\text{e-out}}$ (see Fig. 17(d)). On the one hand, without solder joints, $k_{\text{e-out}}$ of the copper fibres saturated with air decreases by 99.84% in Fig. 17(a). On the other hand, $k_{\text{e-out}}$ of the steel fibre saturated with PCM2 is reduced by only 10.07% in Fig. 17(d). To be conclusive, Fig. 17 reveals that the filling fluids have a grave effect on $k_{\text{e-out}}$ for low-conducting fibres. When the discrepancy in thermal conductivity between the fibre and the filling medium is reduced, the solder joint skips may become a secondary factor affecting out-of-plane heat conduction.

Furthermore, Fig. 18(a)–(d) compare the association between $k_{\text{e-out}}$ and the solder joint skip ratio, where four kinds of fluids, including air, water, PCM1, and PCM2 are filled in the MFMs, respectively. As seen, an increase in ω is often accompanied by a decrease in $k_{\text{e-out}}$. Low-conducting fibre (steel) leads to a moderate decreasing trend for $k_{\text{e-out}}$ with ω, with compared to other metal fibres in Fig. 18. Moreover, this phenomenon becomes more pronounced when the thermal conductivity of the filling medium increases. On the one hand, the variation trend of $k_{\text{e-out}}$ of the four MFMs (Cu, Al, Ni, and steel) is consistent and the difference is slight when the filling medium is air ($k_{air} = 0.0242\text{W}\cdot\text{m}^{-1}\cdot\text{K}^{-1}$). On the other hand, the difference in the variation trend of $k_{\text{e-out}}$ of the fibres becomes visible when the filling medium is PCM2 ($k_{\text{PCM2}} = 3\text{W}\cdot\text{m}^{-1}\cdot\text{K}^{-1}$). For instance, when the filling medium is air with low thermal conductivity, $k_{\text{e-out}}$ of the copper and steel fibre without solder joints are reduced by 99.8% and 96.4% (see Fig. 18(a)), respectively. Likewise, when the filling medium is replaced by PCM2 with high thermal conductivity (Fig. 18(d)), $k_{\text{e-out}}$

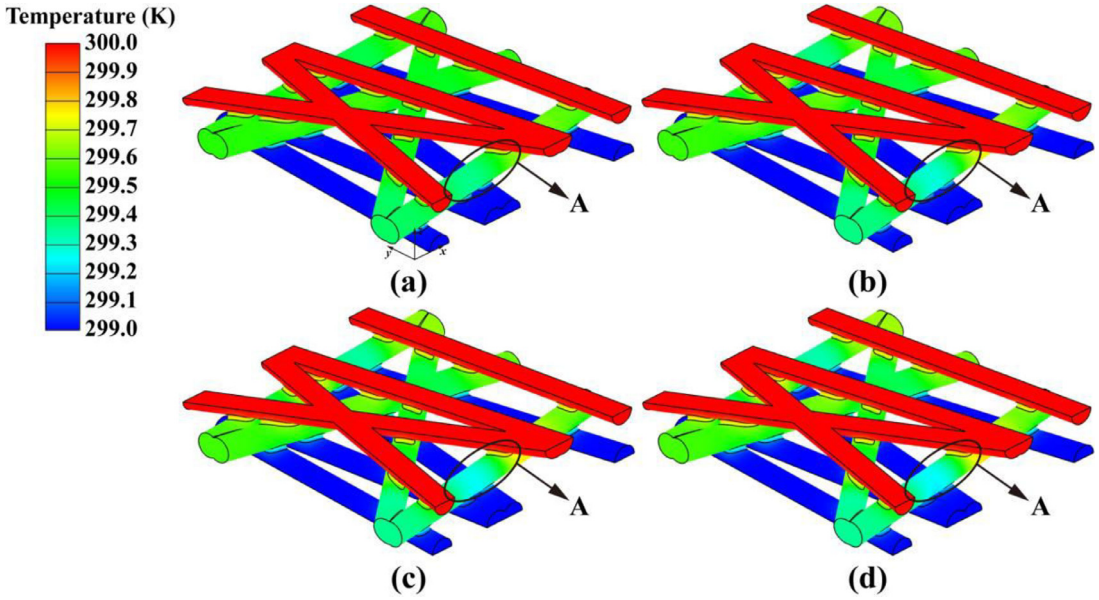

Fig. 16. Temperature distribution for 2-D copper fibre with different thermal conductivity of solder joints: (a) $k_{sf}/k_s = 0.125$; (b) $k_{sf}/k_s = 0.375$; (c) $k_{sf}/k_s = 0.625$; (d) $k_{sf}/k_s = 0.875$.

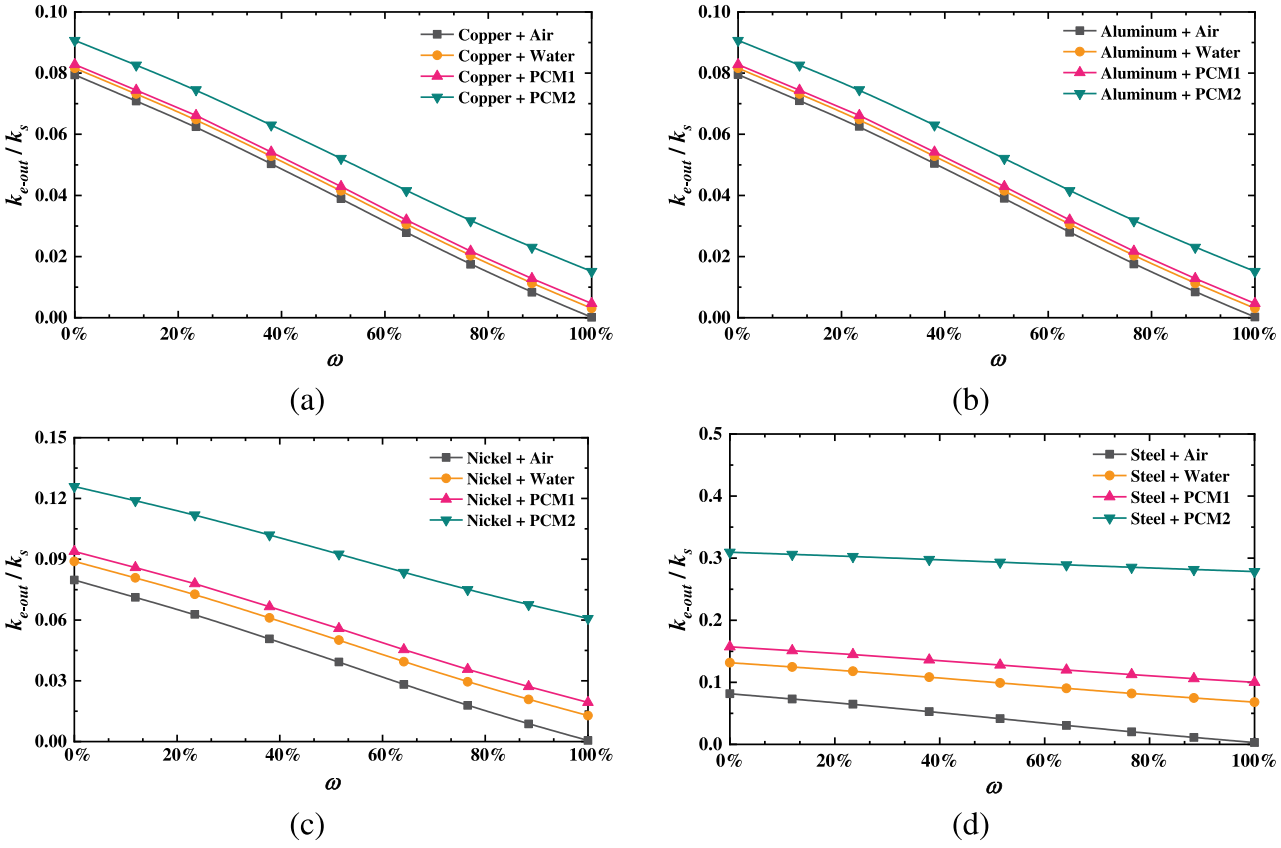

Fig. 17. Comparing the out-of-plane ETC of fibres with different filling fluids: (a) copper; (b) aluminum; (c) nickel; (d) steel.

of the same MFMs decreases by 83.3% and 10.1%, in respective. The influence of the solder joint skips on $k_{\text{e-out}}$ decreases with the increase in the conductivity of the filling medium. As the thermal conductivity of fibres decreases, the impact of the solder joint skips on $k_{\text{e-out}}$ also weakens. In general, the ratio of the thermal conductivity of the filling medium to that of the fiber increases, and the

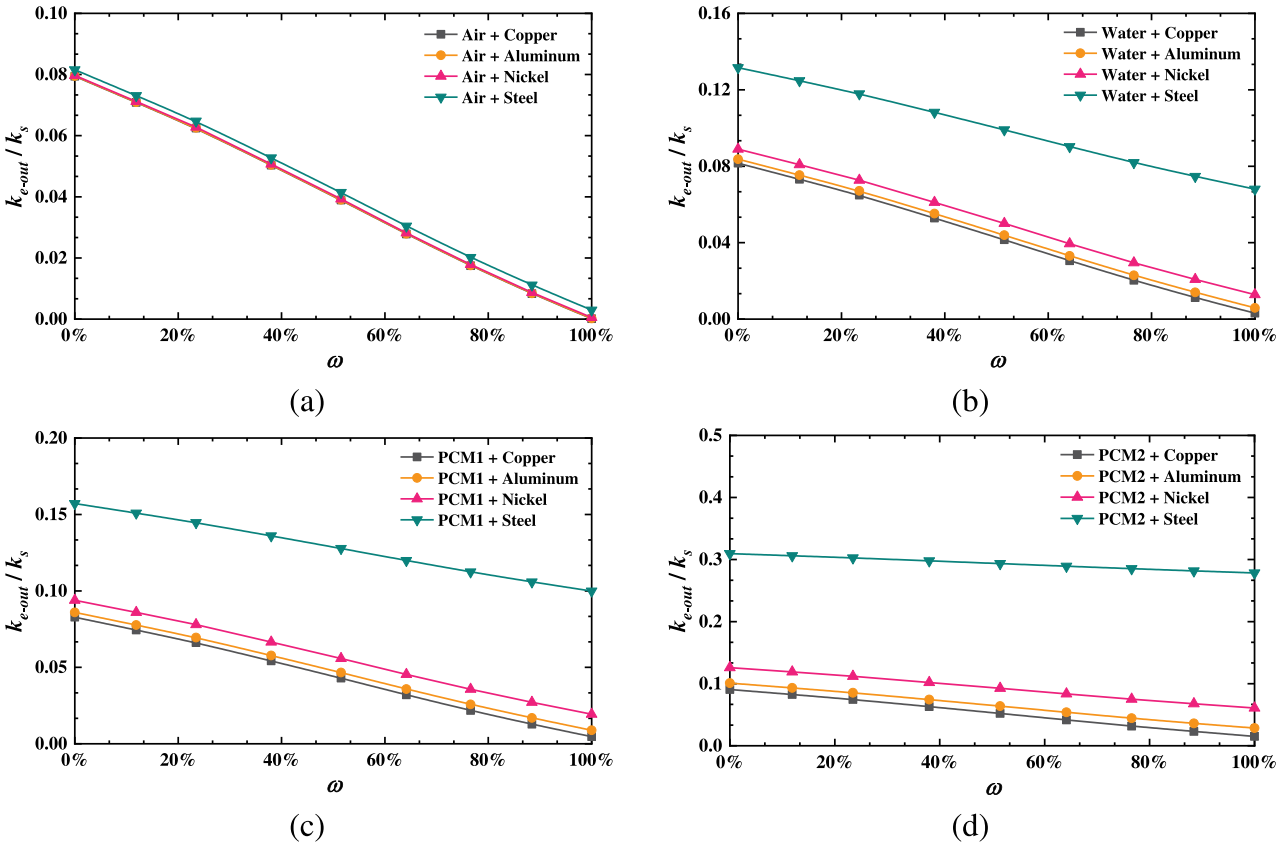

Fig. 18. Comparing the out-of-plane ETC of different fibres with the same filling fluids: (a) air; (b) water; (c) PCM1; (d) PCM2.

effect of the solder joint skips on $k_{e\text{-out}}$ weakens.

5. Conclusion

In this study, the influence mechanisms of the solder joint sizes, the solder joint skips, solder flux materials, and filling fluids on the heat conduction of 2-D random porous fibres are studied. A numerical model is built based on the reconstruction of the microstructure. The numerical model is in satisfactory agreement with the existing data, which verifies the rationality of the numerical simulation. The following conclusions can be drawn:

(1) The dimensionless effective thermal conductivity (ETC) of the porous fibres increases with the solder joint size. As the solder joint ratio increases by 3.06%, the in-plane ($k_{e\text{-in}}$) and out-of-plane ($k_{e\text{-out}}$) dimensionless ETC increase by 9.0% and 437.2%, respectively. In contrast, the solder joint size mainly affects the out-of-plane heat conduction, and the influence on the in-plane heat conduction is subordinate.

(2) An increase in the solder joint skip ratio causes an apparent decline in the ETC of the fibres. Without any solder joint, $k_{e\text{-in}}$ and $k_{e\text{-out}}$ are reduced by an average of 14.3% and 98.8%, respectively. Similarly, the solder joint skips dramatically affect the out-of-plane heat conduction, and their effect on in-plane heat conduction is secondary.

(3) The intact solder joint is a vital factor affecting the out-of-plane heat conduction of the fibres. Furthermore, the distance between the adjoining solder joints of the upper and lower layers is the key factor that cannot be neglected in determining the out-of-plane heat conduction.

(4) The out-of-plane ETC $k_{e\text{-out}}$ of the fibre increases with the thermal conductivity of the solder joints. The increased thermal conductivity of the solder joints enhances heat conduction between the fibre layers.

(5) The influence of the solder joint skips on $k_{e\text{-out}}$ is weakened as the ratio of the thermal conductivity of the filling medium to that of the fiber increases. Without any solder joint, the out-of-plane ETCs of the copper fibre saturated with air and the steel fibre saturated with PCM2 are reduced by 99.8% and 10.1%, respectively. At this point, the ratio of the thermal conductivity of the copper fibre to air is 6.08×10^{-5}, but the ratio of the steel fibre to PCM2 is 0.18.

The current study comprehensively considers the factors affecting the thermal conductivity of 2-D random porous fibers. Quantitative relationships between influencing factors (including the solder joint sizes, the solder joint skips, solder flux materials, and filling fluids) and heat conduction are established by pore-scale simulation. Therefore, the current numerical model can provide reference and guidance for engineering applications.

Declaration of Competing Interest

The authors declare that they have no known competing financial interests or personal relationships that could have appeared to influence the work reported in this paper.

The authors declare the following financial interests/personal relationships which may be considered as potential competing interests.

CRediT authorship contribution statement

Tian Xiao: Formal analysis, Validation, Writing – original draft. **Qiaoling Zhang:** Data curation, Visualization, Writing – review & editing. **Xiaohu Yang:** Conceptualization, Methodology, Writing –

review & editing, Supervision. **Kamel Hooman:** Supervision, Writing – review & editing. **Guodong Li:** Data curation, Supervision.

Data availability

Data will be made available on request.

Acknowledgments

This work was supported by the Open Research Fund Program of State Key Laboratory of Eco-hydraulics in Northwest Arid Region, Xi'an University of Technology (2020KFKT-5), and the National Natural Science Foundation of China (51976155). One of the authors (Xiaohu Yang) gratefully acknowledged the support of K. C. Wong Education Foundation.

References

[1] J.J. Remmers, R. de Borst, A. Needleman, The simulation of dynamic crack propagation using the cohesive segments method, J. Mech. Phys. Solids 56 (1) (2008) 70–92.
[2] A. Vlot, J.W. Gunnink, Fibre Metal Laminates: An Introduction, Springer Science & Business Media, 2011.
[3] R. Alderliesten, R. Benedictus, Fiber/metal composite technology for future primary aircraft structures, J. Aircr. 45 (4) (2008) 1182–1189.
[4] G. Wu, J.M. Yang, The mechanical behavior of GLARE laminates for aircraft structures, JOM 57 (1) (2005) 72–79.
[5] E.C. Botelho, R.A. Silva, L.C. Pardini, M.C. Rezende, A review on the development and properties of continuous fiber/epoxy/aluminum hybrid composites for aircraft structures, Mater. Res. 9 (3) (2006) 247–256.
[6] G. Wu, Y. Tan, J.M. Yang, Evaluation of residual strength of notched fiber metal laminates, Mater. Sci. Eng. A 457 (1–2) (2007) 338–349.
[7] T. Lu, H.A. Stone, M. Ashby, Heat transfer in open-cell metal foams, Acta Mater. 46 (10) (1998) 3619–3635.
[8] L. Tadrist, M. Miscevic, O. Rahli, F. Topin, About the use of fibrous materials in compact heat exchangers, Exp. Therm. Fluid Sci. 28 (2–3) (2004) 193–199.
[9] S. Mahjoob, K. Vafai, A synthesis of fluid and thermal transport models for metal foam heat exchangers, Int. J. Heat Mass Transf. 51 (15–16) (2008) 3701–3711.
[10] C. Zhao, M. Opolot, M. Liu, F. Bruno, S. Mancin, K. Hooman, Numerical study of melting performance enhancement for PCM in an annular enclosure with internal-external fins and metal foams, Int. J. Heat Mass Transf. 150 (2020) 119348.
[11] H. Pourrahmani, M. Moghimi, M. Siavashi, Thermal management in PEMFCs: the respective effects of porous media in the gas flow channel, Int. J. Hydrogen Energy 44 (5) (2019) 3121–3137.
[12] J.H. Lin, Novel compound cushion layer for reinforcement of ballistic resistance, Textile Res. J. 75 (5) (2005) 431–436.
[13] F. Martínez-Hergueta, A. Ridruejo, F. Gálvez, C. González, J. LLorca, Influence of fiber orientation on the ballistic performance of needlepunched nonwoven fabrics, Mech. Mater. 94 (2016) 106–116.
[14] M.A. Choi, M.H. Lee, J. Chang, S.J. Lee, Permeability modeling of fibrous media in composite processing, J. Non Newton. Fluid Mech. 79 (2–3) (1998) 585–598.
[15] B.T. Åström, R.B. Pipes, S.G. Advani, On flow through aligned fiber beds and its application to composites processing, J. Compos. Mater. 26 (9) (1992) 1351–1373.
[16] J. Feser, A. Prasad, S.G. Advani, Experimental characterization of in-plane permeability of gas diffusion layers, J. Power Sources 162 (2) (2006) 1226–1231.
[17] J.T. Gostick, M.W. Fowler, M.A. Ioannidis, M.D. Pritzker, Y.M. Volfkovich, A. Sakars, Capillary pressure and hydrophilic porosity in gas diffusion layers for polymer electrolyte fuel cells, J. Power Sources 156 (2) (2006) 375–387.
[18] M.M. Heyhat, S. Mousavi, M. Siavashi, Battery thermal management with thermal energy storage composites of PCM, metal foam, fin and nanoparticle, J. Energy Storage 28 (2020) 101235.
[19] D.M. Burke, M.A. Morris, J.D. Holmes, Chemical oxidation of mesoporous carbon foams for lead ion adsorption, Sep. Purif. Technol. 104 (2013) 150–159.
[20] G. Liu, Z. Du, T. Xiao, J. Guo, L. Lu, X. Yang, K. Hooman, Design and assessments on a hybrid pin fin-metal foam structure towards enhancing melting heat transfer: an experimental study, Int. J. Therm. Sci. 182 (2022) 107809.
[21] T. Xiao, G. Liu, J. Guo, G. Shu, L. Lu, X. Yang, Effect of metal foam on improving solid–liquid phase change in a multi-channel thermal storage tank, Sustain. Energy Technol. Assess. 53 (2022) 102533.
[22] M. Pan, Y. Zhong, Experimental and numerical investigation of a thermal management system for a Li-ion battery pack using cutting copper fiber sintered skeleton/paraffin composite phase change materials, Int. J. Heat Mass Transf. 126 (2018) 531–543.
[23] Z. Chen, G. Fang, J. Xie, J. Liang, Experimental study of high-temperature tensile mechanical properties of 3D needled C/C–SiC composites, Mater. Sci. Eng. A 654 (2016) 271–277.
[24] T.T. Li, R. Wang, C.W. Lou, J.H. Lin, Evaluation of high-modulus, puncture-resistance composite nonwoven fabrics by response surface methodology, J. Ind. Textiles 43 (2) (2013) 247–263.
[25] T. Xiao, J. Guo, X. Yang, K. Hooman, T.J. Lu, On the modelling of heat and fluid transport in fibrous porous media: analytical fractal models for permeability and thermal conductivity, Int. J. Therm. Sci. 172 (2022) 107270.
[26] Y. Mahmoudi, K. Hooman, K. Vafai, Convective Heat Transfer in Porous Media, CRC Press, 2019.
[27] J. Xie, J. Fang, L. Chen, W. Jiao, Z. Yang, L. Chen, Micro-scale modeling of 3D needled nonwoven fiber preforms, Compos. Struct. 281 (2022) 114995.
[28] P.H. Jadhav, T. G, N. Gnanasekaran, M. Mobedi, Performance score based multi-objective optimization for thermal design of partially filled high porosity metal foam pipes under forced convection, Int. J. Heat Mass Transf. 182 (2022) 121911.
[29] E. Sadeghi, M. Bahrami, N. Djilali, Analytic determination of the effective thermal conductivity of PEM fuel cell gas diffusion layers, J. Power Sources 179 (1) (2008) 200–208.
[30] Z. Qu, T. Wang, W. Tao, T. Lu, A theoretical octet-truss lattice unit cell model for effective thermal conductivity of consolidated porous materials saturated with fluid, Heat Mass Transf. 48 (8) (2012) 1385–1395.
[31] T. Xiao, X. Yang, K. Hooman, L. Jin, C. Yang, T.J. Lu, Conductivity and permeability of graphite foams: analytical modelling and pore-scale simulation, Int. J. Therm. Sci. 179 (2022) 107706.
[32] A.N. Volkov, L.V. Zhigilei, Thermal conductivity of two-dimensional disordered fibrous materials defined by interfiber thermal contact conductance and intrinsic conductivity of fibers, J. Appl. Phys. 127 (6) (2020) 065102.
[33] M. Wang, J. He, J. Yu, N. Pan, Lattice Boltzmann modeling of the effective thermal conductivity for fibrous materials, Int. J. Therm. Sci. 46 (9) (2007) 848–855.
[34] R. Arambakam, H.V. Tafreshi, B. Pourdeyhimi, A simple simulation method for designing fibrous insulation materials, Mater. Des. 44 (2013) 99–106.
[35] X. Huang, Q. Zhou, J. Liu, Y. Zhao, W. Zhou, D. Deng, 3D stochastic modeling, simulation and analysis of effective thermal conductivity in fibrous media, Powder Technol. 320 (2017) 397–404.
[36] L. Ni, Z. Chen, P. Mukhopadhyaya, X. Zhang, Q. Wu, Q. Yu, G. Miu, Numerical simulation on thermal performance of vacuum insulation panels with fiber/powder porous media based on CFD method, Int. J. Therm. Sci. 172 (2022) 107320.
[37] M. Siavashi, S.M. Miri Joibary, Numerical performance analysis of a counter-flow double-pipe heat exchanger with using nanofluid and both sides partly filled with porous media, J. Therm. Anal. Calorimetry 135 (2) (2019) 1595–1610.
[38] C. Veyhl, T. Fiedler, O. Andersen, J. Meinert, T. Bernthaler, I. Belova, G. Murch, On the thermal conductivity of sintered metallic fibre structures, Int. J. Heat Mass Transf. 55 (9–10) (2012) 2440–2448.
[39] N. Haruki, A. Horibe, K. Nakashima, Anisotropic effective thermal conductivity measurement of various kinds of metal fiber materials, Int. J. Thermophys. 34 (12) (2013) 2385–2399.
[40] W. Li, Z. Qu, Experimental study of effective thermal conductivity of stainless steel fiber felt, Appl. Therm. Eng. 86 (2015) 119–126.
[41] P. Yi, L. Peng, X. Lai, M. Li, J. Ni, Investigation of sintered stainless steel fiber felt as gas diffusion layer in proton exchange membrane fuel cells, Int. J. Hydrogen Energy 37 (15) (2012) 11334–11344.
[42] K. Hooman, N. Dukhan, A theoretical model with experimental verification to predict hydrodynamics of foams, Transp. Porous Media 100 (3) (2013) 393–406.
[43] M. Sheng, D.R. Cahela, H. Yang, C.F. Gonzalez, W.R. Yantz Jr, D.K. Harris, B.J. Tatarchuk, Effective thermal conductivity and junction factor for sintered microfibrous materials, Int. J. Heat Mass Transf. 56 (1–2) (2013) 10–19.
[44] H. Moghimi, M. Siavashi, M. Mousavi Nezhad, A. Guadagnini, Pore-scale computational analyses of non-Darcy flow through highly porous structures with various degrees of geometrical complexity, Sustain. Energy Technol. Assess. 52 (2022) 102048.
[45] P. Poureslami, M. Siavashi, H. Moghimi, M. Hosseini, Pore-scale convection–conduction heat transfer and fluid flow in open-cell metal foams: a three-dimensional multiple-relaxation time lattice Boltzmann (MRT-LBM) solution, Int. Commun. Heat Mass Transf. 126 (2021) 105465.
[46] M. Ramezanpour, M. Siavashi, A.Q. Raeini, M.J. Blunt, Pore-scale simulation of nanoparticle transport and deposition in a microchannel using a Lagrangian approach, J. Mol. Liquids 355 (2022) 118948.
[47] E. Sepehri, M. Siavashi, Pore-scale direct numerical simulation of fluid dynamics, conduction and convection heat transfer in open-cell Voronoi porous foams, Int. Commun. Heat Mass Transf. 137 (2022) 106274.
[48] M. Shirbani, M. Siavashi, M. Hosseini, M. Bidabadi, Improved thermal energy storage with metal foam enhanced phase change materials considering various pore arrangements: a pore-scale parallel lattice Boltzmann solution, J. Energy Storage 52 (2022) 104744.
[49] T. Fiedler, N. White, M. Dahari, K. Hooman, On the electrical and thermal contact resistance of metal foam, Int. J. Heat Mass Transf. 72 (2014) 565–571.
[50] M. Opolot, C. Zhao, M. Liu, S. Mancin, F. Bruno, K. Hooman, Investigation of the effect of thermal resistance on the performance of phase change materials, Int. J. Therm. Sci. 164 (2021) 106852.
[51] S. Maneemuang, N. Kammuang-Lue, P. Terdtoon, P. Sakulchangsatjatai, Effect of pipe flattening on pressure drop in vapor core and thermal characteristic of miniature round and flat-shape heat pipe with sintered fiber wick, Int. J. Heat Mass Transf. 176 (2021) 121416.
[52] J.M. Charles, Performance and Stability of $CaCl_2 \cdot 6H_2O$-Based Phase Change Materials, Lehigh University, 2019.
[53] R. Ye, W. Lin, X. Fang, Z. Zhang, A numerical study of building integrated

with $CaCl_2 \cdot 6H_2O$/expanded graphite composite phase change material, Appl. Therm. Eng. 126 (2017) 480–488.
[54] J. Sun, Z. Hu, J. Li, H. Zhang, C. Sun, Thermal and mechanical properties of fibrous zirconia ceramics with ultra-high porosity, Ceram. Int. 40 (8) (2014) 11787–11793.
[55] J.T. Gostick, M.W. Fowler, M.D. Pritzker, M.A. Ioannidis, L.M. Behra, In-plane and through-plane gas permeability of carbon fiber electrode backing layers, J. Power Sources 162 (1) (2006) 228–238.